

Versatile Post-Doping toward Two-Dimensional Semiconductors

Yuya Murai, Shaochun Zhang, Takato Hotta, Zheng Liu, Takahiko Endo, Hiroshi Shimizu, Yasumitsu Miyata, Toshifumi Irisawa, Yanlin Gao, Mina Maruyama, Susumu Okada, Hiroyuki Mogi, Tomohiro Sato, Shoji Yoshida, Hidemi Shigekawa, Takashi Taniguchi, Kenji Watanabe, Ruben Canton-Vitoria, and Ryo Kitaura*



Cite This: *ACS Nano* 2021, 15, 19225–19232



Read Online

ACCESS |



Metrics & More



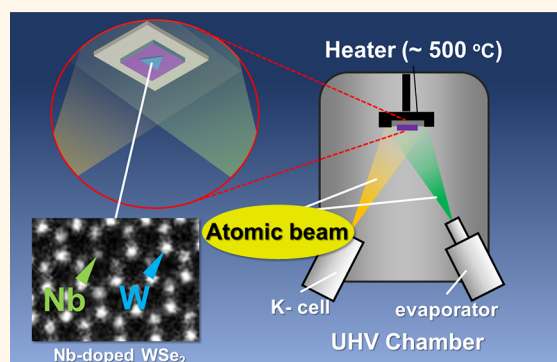
Article Recommendations



Supporting Information

ABSTRACT: We have developed a simple and straightforward way to realize controlled postdoping toward 2D transition metal dichalcogenides (TMDs). The key idea is to use low-kinetic-energy dopant beams and a high-flux chalcogen beam simultaneously, leading to substitutional doping with controlled dopant densities. Atomic-resolution transmission electron microscopy has revealed that dopant atoms injected toward TMDs are incorporated substitutionally into the hexagonal framework of TMDs. The electronic properties of doped TMDs (Nb-doped WSe_2) have shown drastic change and *p*-type action with more than 2 orders of magnitude increase in current. Position-selective doping has also been demonstrated by the postdoping toward TMDs with a patterned mask on the surface. The postdoping method developed in this work can be a versatile tool for 2D-based next-generation electronics in the future.

KEYWORDS: two-dimensional materials, doping, transistors, STEM, transition metal dichalcogenides



The current limitation in Si-based devices, arising from the adverse short-channel effect, has led to searching for materials for next-generation electronic devices. The short-channel effect becomes serious when the electric field originating from the source/drain electrodes is comparable to that of the gate electrode. In this case, the gate electric field cannot control the channel current properly, and adverse effects, such as a decrease of threshold voltage and degradation of subthreshold characteristics, inevitably emerge. Various approaches, including double-gate field-effect transistors (FETs) and FinFET, are now being investigated to overcome the short-channel effect.^{1,2} Among the various approaches, one of the promising ways is to use new material, particularly atomically thin semiconductors (two-dimensional (2D) semiconductors), as semiconductor channels.^{3,4}

The discovery of 2D semiconductors has triggered research toward next-generation nanoelectronics.^{5,6} Research on 2D materials started with gapless graphene, and graphene research soon led to the isolation of various 2D semiconductors, such as transition metal dichalcogenides (TMDs, for example, MoS_2 , WSe_2 , etc.), whose band gap ranges in energy from 1 to 2 eV.^{7,8} 2D semiconductors possess a uniform thickness of less than 1 nm without, ideally, any dangling bonds at the surface, and the

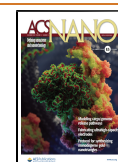
ultrathin uniform structure of 2D semiconductors is ideal to realize ultrashort-channel devices. Past research on 2D semiconductors has already demonstrated that 2D semiconductors work as high on/off ratio FETs with carrier mobility up to the order of $10^2 \text{ cm}^2/(\text{V s})$ at room temperature.^{9–11} In conjunction with the recent advancement of growth techniques and the successful formation of ohmic contacts, 2D semiconductors provide an excellent opportunity to develop next-generation nanoelectronics.^{12,13}

The accurate postdoping method for 2D materials is crucial for the development of 2D-material-based electronic devices. The success in Si devices is based on reliable postdoping techniques; *p/n*-doped Si works as electrodes/channels in Si-based metal-oxide-semiconductor FETs (MOSFETs) in integrated circuits. In the fabrication of Si MOSFETs, *p/n* dopants are incorporated through ion implantation or diffusion, forming

Received: May 30, 2021

Accepted: November 22, 2021

Published: November 29, 2021



electrodes and channels at desired locations. However, the same technique cannot be applied for doping into 2D semiconductors because high-energy ions or high-temperature diffusion processes can damage the ultrathin structure of 2D semiconductors. Doping toward 2D materials has, therefore, been performed through mixing dopants during growth processes.^{14–19} Using this method, various dopants, such as Re and Nb, have been successfully doped to show *p/n*-type FET characteristics.^{16,20} Although this is a versatile way to dope *p/n* dopants substitutionally to frameworks of 2D materials, the development of accurate postdoping is essential to realize position-controlled doping for future 2D-semiconductor-based devices.

In this work, we have developed a straightforward way to realize controlled postdoping toward 2D transition metal dichalcogenides (TMDs), including MoSe₂, WSe₂, *etc.* Figure 1 shows a schematic representation of the doping process

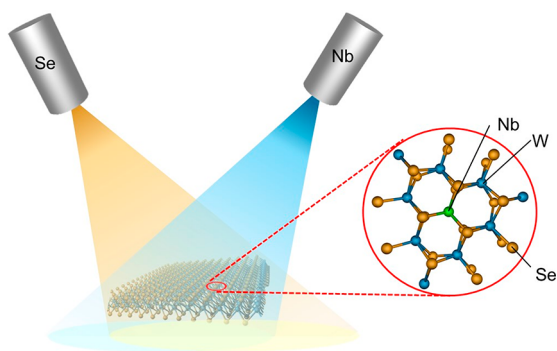


Figure 1. Schematic representation of the postdoping process. A predeposited crystal of TMD (in this case, WSe₂) is irradiated with a dopant (Nb) and a chalcogen (Se) beam, which leads to substitutional postdoping of Nb toward WSe₂.

developed in this work. The key idea is to use dopant beams (Nb, Re, *etc.*) with low kinetic energy generated by thermal evaporation of high-melting-point metals. The kinetic energy distribution $P(E_{\text{kin}}, \beta)$ of atoms in dopant beams is expected to be proportional to $\exp(-\beta E_{\text{kin}})$, where E_{kin} and β represent kinetic energy and inverse temperature ($1/k_{\text{B}}T$; k_{B} , Boltzmann constant; T , temperature), respectively. In high-melting-point metals, such as Nb and Re, we need a temperature around the melting point (2750 and 3458 K for Nb and Re) to have a beam flux high enough for doping processes. In this case, the distribution of E_{kin} ranges typically from several hundreds of meV to 1–2 eV, leading to substitutional doping without significantly damaging the original framework of host 2D semiconductors. Also, we supply a Se beam with a high flux rate (Se/Nb > 3000) during the whole doping process to heal Se vacancies and enhance structural reconstruction to form well-regulated substitutionally doped TMDs. In this method, accurate and position-selective doping becomes possible through accurate control of the dopant beam flux with a mask layer patterned on 2D TMDs.

RESULTS AND DISCUSSION

Figure 2a and b shows atomic-resolution high-angle annular dark-field (HAADF)-scanning transmission electron microscope (STEM) images of a monolayer of WSe₂ after 3- and 6-min exposures of niobium (Nb) beams with a flux of 0.67 monolayer/hour. Although optical images show almost no

change after the doping process (Figure S1), HAADF-STEM images show significant change. Spotlike contrasts observed in the images can be roughly categorized into three groups: the brightest, the middle, and the darkest ones. The brightest and the middle ones correspond to W and two Se atoms standing vertically, respectively. The darkest contrasts observed at the W positions correspond to Nb atoms substituted into the framework of WSe₂. Also, image contrasts darker than those of Nb are seen at Se sites (Figure 2d shows one dark spot at a Se site), probably originating from single Se vacancies; single Se vacancies arise not only from the growth process of WSe₂ but also from the formation of Se defects induced by electron beam irradiation.²¹ In HAADF-STEM images, image contrasts strongly depend on the atomic number (*Z*-contrast), and substitutions of W by Nb are expected to yield darker contrasts than W, as seen in the HAADF-STEM images. Figure 2c and d shows cutouts from the white squares shown in Figure 2a and b, respectively. The hexagonal network structure of WSe₂ is clearly visible, and dark contrasts at W sites are assigned to Nb atoms substituted to W sites as shown in the structure models in Figure 2c and d. To confirm the assignment, we performed STEM image simulations using WinHREM software (HREM Research). As seen in Figure 2e, the simulated image well matches the observed one shown in Figure 2c. Also, the line profiles along the direction indicated by the blue arrows in Figure 2c and e agree well (Figure 2f: left, observed; right, simulated), which further confirms the substitution of W by Nb.²² We carefully checked the HAADF-STEM images and found that no W or Nb atoms exist on top of the 2D layers; the additional contrast from surface adsorbed W/Nb atoms has not been observed in any HAADF-STEM images. Energy-dispersive X-ray spectroscopy has revealed that the Nb atoms are distributed uniformly over the WSe₂ samples (Figure S2). Substitution of Se by Nb is energetically unfavorable, and therefore, Nb atoms should predominantly occupy W sites in the current doping process. Direct counting the number of Nb atoms substituted gives doping rates of 3.4 and 7.4 at % for 3- and 6-min exposures, respectively; the corresponding doping rate, in this case, is 1.2 at %/min. Because the determined doping rate is slow enough, it is possible to control the degree of doping precisely, and we can easily make the doping rate slower just by using smaller Nb flux in this method.

Whereas most Nb atoms are isolated to form one-atom-sized dark contrasts in Figure 2a and b, some Nb atoms form clusters in WSe₂ (particularly in Figure 2a). To see if Nb substituted in WSe₂ favors the formation of clusters or not, we calculated the alloying degree J , defined as follows.^{23,24}

$$J_{\text{W}} = P_{\text{obs}}/P_{\text{rand}} \times 100\%$$

where P_{obs} and P_{rand} represent the averaged number of Nb adjacent to a W atom and the atomic ratio of Nb in the examined region, respectively; concrete representations of P_{obs} and P_{rand} are given in the Supporting Information. Whereas a J_{W} of 100% means no preference in neighboring atoms for Nb substituted in WSe₂, J_{W} smaller/larger than 100% means Nb atoms prefer isolation/clustering. Counting 300 Nb atoms yields J_{W} of 97 and 92% for doping rates of 3.4 and 7.4 at %, respectively, suggesting that the present Nb substitution occurs almost randomly. The observed random doping indicates that Nb atoms may exist as single atoms or tiny clusters composed of 2–3 atoms in Nb beams, and after landing on a WSe₂ layer, Nb atoms are immediately incorporated into the WSe₂ layer without significant surface diffusion to form large Nb clusters.

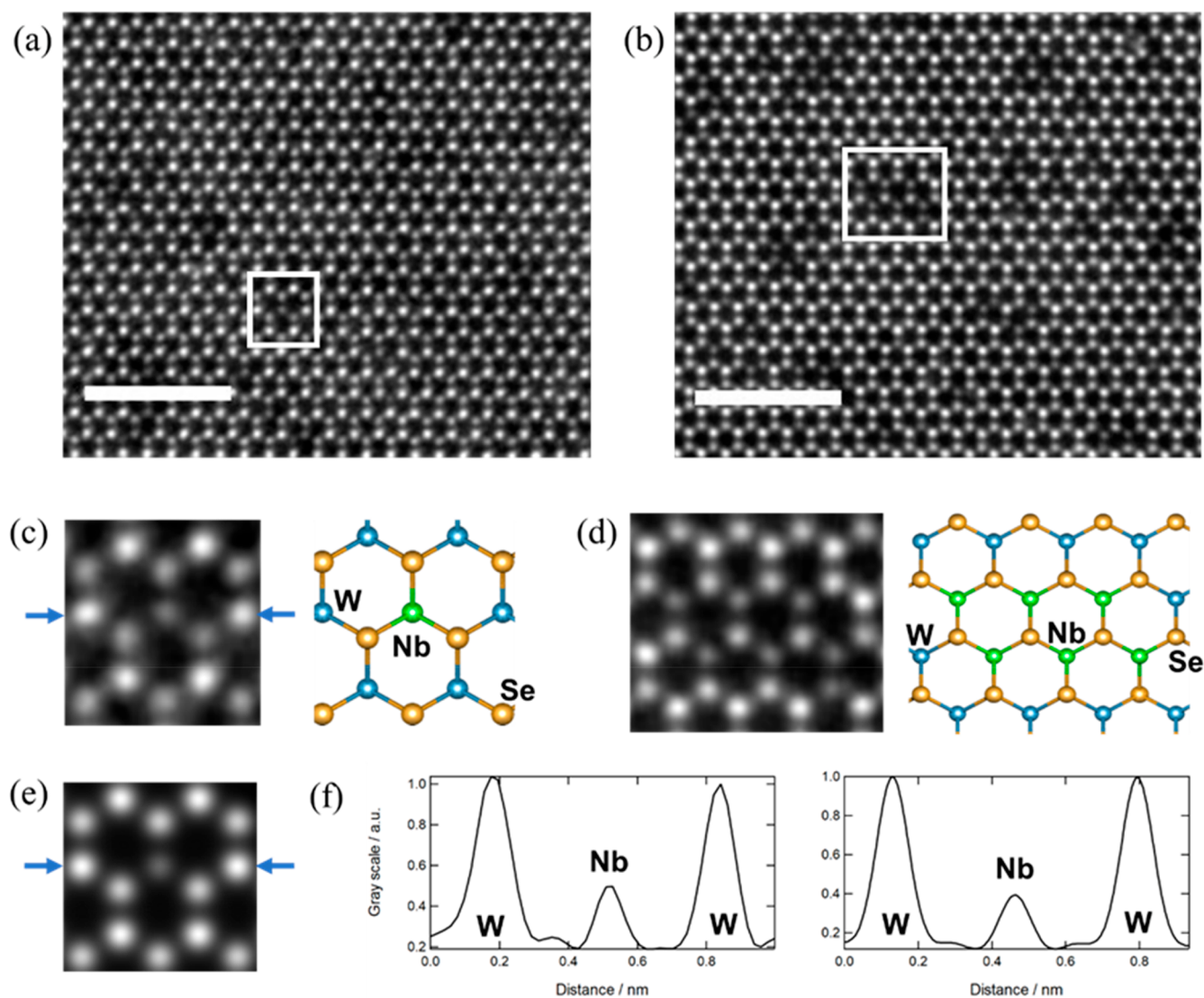


Figure 2. (a and b) Typical HAADF-STEM images of monolayer WSe_2 after 3- and 6-min doping of Nb. After applying “subtract background” with a rolling ball radius of 2 nm, a bandpass filter was applied to filter out large and small structures, whose sizes are 2 and 0.06 nm, respectively. All these image processings were performed with ImageJ.²⁵ The scale bars correspond to 2 nm. (c and d) Cutouts from the white squares in parts a and b, respectively. Corresponding structure models are also shown. In the structure models, blue, green, and yellow balls correspond to W, Nb, and Se atoms, respectively. (e) Image simulated with the structure model shown in part c. (f) Line profiles of the simulated (right) and the observed (left) HAADF-STEM images shown in parts c and e. The line profiles were made along the direction indicated by the blue arrows shown in parts c and e.

Figure 3a shows room-temperature photoluminescence (PL) spectra of monolayer WSe_2 before and after a 6-min Nb beam exposure. As clearly demonstrated, the doping process causes a significant decrease in PL intensity; the PL peak arises from radiative recombination of bright excitons at the K/-K valley. The observed reduction in PL intensity is consistent with carrier doping induced by the substitutional doping reported previously.^{17,26–28} In addition to the decrease in PL intensity, PL peaks shift to the red side, which is consistent with the previous works on substitutional Nb doping; the increase in hole density and possible strain induced by Nb doping can cause the PL red shift.²⁸ Corresponding Raman spectra (Figure 3b), where Raman peaks arising from A'_1 and E' at around 250 cm^{-1} are seen, showing intensity reduction, also compatible with earlier works.^{17,29} Typical AFM image and height profiles before and after doping (Figure 3c) show that the thickness of the original WSe_2 does not alter after a doping process; the

formation of second layers, metallic NbSe_2 , and attachment of impurities are not observed. X-ray photoelectron spectroscopy (XPS) has shown the existence of Nb atoms (Nb 3d peaks) and doping-induced red shifts in the W 4f and Se 3d peaks in the XPS spectra of Nb-doped WSe_2 , which is consistent with previous works (Figure S3).^{20,28} Considering all results, including HAADF-STEM, EDX, PL, AFM, and XPS, it is reasonable to conclude that substitutional Nb doping, which leads to hole doping, is the dominant process in our postdoping method.

To address the mechanism of the present doping process, we have performed an *ab initio* molecular dynamics (MD) simulation, where an Nb atom with a kinetic energy of about 300 meV is injected toward a monolayer of WSe_2 (similar results were obtained with different kinetic energies, Figure S4). Figure 4 shows snapshots of the structural change upon the injection (a movie is available as a Supporting Information movie file). As seen in the snapshots, the Nb atom hits a W atom, followed by

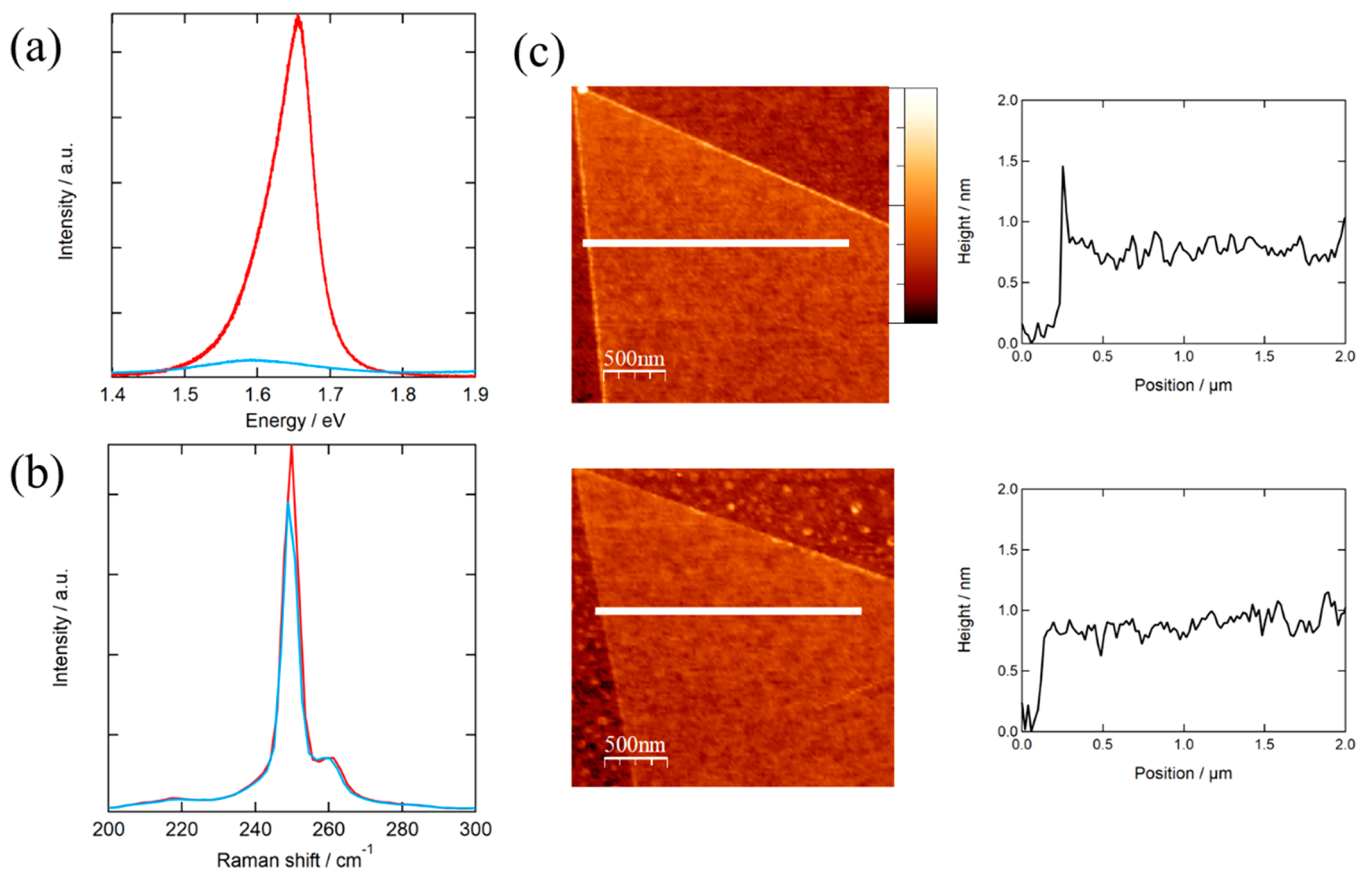


Figure 3. (a, b, and c) Typical PL, Raman spectra, and AFM images/height profiles of a pristine monolayer of WSe₂ and the monolayer of WSe₂ after 6-min doping of Nb. Red and blue curves correspond to spectra of the pristine sample and Nb-doped sample, respectively. We used the excitation wavelength of 532 nm to measure the PL and Raman spectra. Intensities of the Raman spectra are normalized by the Si peak at 520 cm⁻¹. The maximum and minimum heights shown by the color scale in part c are 4.5 and 0 nm, respectively. The AFM height profiles correspond to the height along the white lines shown in part c.

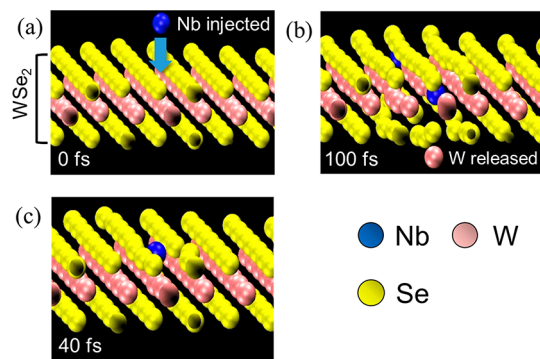


Figure 4. Snapshots of the *ab initio* molecular dynamics simulation of Nb atom injected toward monolayer WSe₂. Parts a, b, and c show a snapshot after 0, 40, and 100 fs, respectively.

the release of the W atom from the original position. The W atom released moves around the original position during the simulation time (3 ps). As mentioned above, we observed no W or Nb atom on the WSe₂ layer after doping processes, which means that released W atoms are incorporated into the WSe₂ again. We perform the doping at 823 K with the supply of Se with a high flux rate of 2 Å/s (Se/Nb > 3000), and structural reconstruction to recover the original hexagonal network occurs under this condition. The high-flux Se supply during the doping processes is probably essential to form the hexagonal network structure because injecting Nb atoms alone results in the

formation of not the hexagonal network but mirror twin boundaries.³⁰ As seen in the *ab initio* MD calculation, Nb atoms injected are rapidly incorporated into WSe₂ without significant surface diffusion. In this case, the formation of Nb clusters is not likely, which is consistent with the analyses of STEM images, random Nb doping.

One of the advantages of the present doping method is position-controlled doping. For this purpose, we deposit a patterned mask on a monolayer of WSe₂ by electron beam lithography with an inorganic resist (Hydrogen Silsesquioxane, HSQ); HSQ is stable up to a process temperature of 823 K. Figure 5 shows optical and Raman images of WSe₂ with an HSQ pattern after 6-min doping. The green and orange frames in Figure 5a show a monolayer of WSe₂ on a hBN flake and HSQ patterns (rectangular bars) fabricated on WSe₂/hBN. To confirm the spatial distribution of the Nb-doped area, we have performed Raman intensity mapping (Figure 5b), where image contrasts correspond to Raman intensity. As clearly seen, the region exposed to the dopant beam shows quenching of Raman intensity, whereas the region covered by the HSQ patterns gives strong Raman intensity, giving the dark/bright contrasts pattern in the Raman image shown in Figure 5b. The observed pattern in the Raman image matches the HSQ pattern well, consistent with spatially selective Nb doping via HSQ patterning. The spatially selective doping is expected because the doping processes are performed at 823 K, which is low enough to inhibit the thermal diffusion of doped Nb atoms in the framework of WSe₂. Given

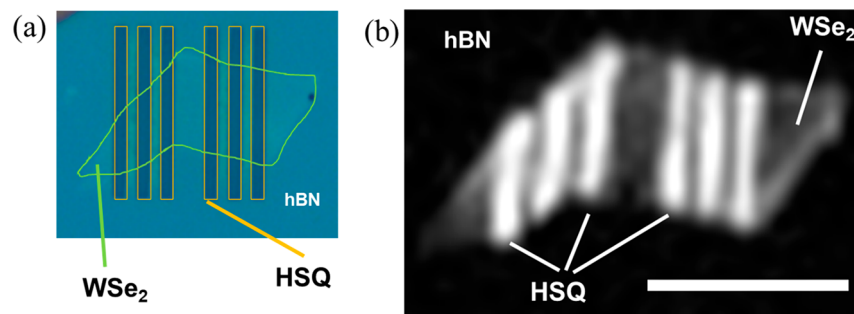


Figure 5. (a) Optical microscope image and (b) corresponding Raman image of patterned Nb-doped WSe₂. Raman intensities from A₁' and 2LA are used to make the Raman image. We used a Nb doping ratio larger than 10 at % to enhance the difference in Raman intensity for this measurement. The scale bar corresponds to 10 μm. The excitation wavelength 532 nm, the excitation power 30.8 μW, and the exposure time 30 s were used to obtain the Raman image. The Raman intensity is displayed by grayscale from 0–18000 counts.

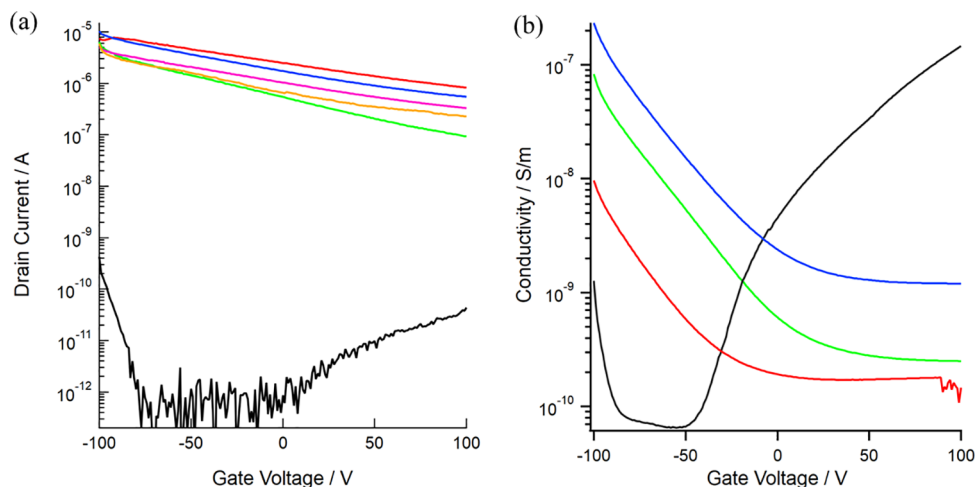


Figure 6. (a) Transfer curves of monolayer WSe₂ measured at room temperature. All devices are on the same substrate, and 6-min Nb doping was performed before the measurements. The black curve represents a typical transfer curve of monolayer WSe₂ before the doping. Red, blue, pink, yellow, and green curves correspond to transfer curves of FET devices (after 6-min doping) located at different positions in a substrate. We use channel length = 20 μm and channel width = 20 μm in this measurement. (b) Transfer curves of pristine multilayer WSe₂ (black) and WSe₂ after 1-min (red), 2-min (green), and 3-min doping (blue). All transfer curves were measured at room temperature with a bias voltage of 10 V (channel length = 20 μm, channel width = 67 μm).

that lateral TMD heterostructures grown at high temperatures (~1000 K) give sharp junction interfaces, the temperature needed for thermal diffusion within the framework is supposed to be much higher than the temperature in the current doping processes.^{31,32} The high-temperature required for the thermal diffusion means that substitutional doping with nanometer-scale precision is possible in the current method, leading to the possibility of realizing arrays of FETs with ultrashort 2D channels in the future.

Figure 6a shows two-terminal transfer curves of WSe₂ before and after a 6-min exposure to a Nb beam; we used five monolayer WSe₂ grown on a SiO₂/Si substrate for this Nb doping. The *ab initio* band structure calculation of Nb-doped WSe₂ (Figure S5) shows that the Nb atom doped yields a localized state around the VBM of WSe₂, showing that Nb should work as a *p*-dopant. As seen in the transfer curves shown in Figure 6a, the on current (I_{on}) before doping is very small, typically ~100 pA, probably due to considerable contact resistance from the Schottky barrier at the interface between Ti and WSe₂. In contrast, after doping, I_{on} is greatly enhanced in all cases, typically four orders in magnitude, and all devices clearly show *p*-type behavior consistent with previous works (Figure 6a).^{16,33,34} The observed I_{on} increase should originate

from lowering the Schottky barrier induced by the increase in hole density. The *p*-doping was also confirmed by an upward shift of Fermi energy in angle-resolved photoelectron spectra and scanning tunneling microscopy/spectroscopy (Figures S6 and S7). A critical point here is that *p*-type doping occurs uniformly all over the substrate because of the uniform intensity of Nb dopant beams; the current size of the Nb beam is at least 2 cm, which is larger than those of the substrate used.

Because the present doping method is a postdoping method, it should be possible to increase the number of dopants afterward. Figure 6b shows a transfer curve of a pristine bilayer of WSe₂ and transfer curves of the same bilayer of WSe₂ after several consecutive Nb postdoping processes; electrodes can work even after multiple times Nb postdoping processes. As seen in Figure 6a, all transfer curves show explicit *p*-type action, and I_{on} increases in a stepwise manner as the doping process was repeated, finally reaching 10⁻⁶ A after three times doping; additional doping led to a decrease in I_{on} , probably due to increased Coulomb scatterings from increased impurities. The observed increase in I_{on} demonstrates that we can tune the Nb doping ratio afterward, making the present postdoping method useful to fabricate various functional devices. One more critical point of the present postdoping method is that the same process

should be transferred to dope various dopants to 2D semiconductors; dopant atoms are expected to be doped regardless of kinds of atoms unless atoms possess sufficient kinetic energy/momentum. We also performed Re doping with a Re beam to demonstrate this transferability and found that the postdoping method developed also works for Re doping (Figure S8). PL spectra before and after Re doping show results similar to those obtained in the Nb doping, where the decrease in PL intensity is seen after Re doping. A HAADF-STEM image of a Re doped sample shows a bright spot at a metal site, which is also consistent with Re doping; we used MoSe₂ to visualize doped Re atoms. The FET characteristic shows *n*-type action after the doping, which is expected in the case of Re doping.³⁵

CONCLUSION

In conclusion, we have successfully developed a postdoping method for 2D semiconductors, including MoSe₂ and WSe₂. The key idea is to simultaneously use a low-energy dopant beam and a high-flux chalcogen beam, leading to accurate post doping of p/n dopants substitutionally into 2D structures. Atomic-resolution HAADF-STEM observations and *ab initio* molecular dynamics simulations have revealed that low-energy dopant atoms can be directly incorporated without damaging the original lattice to achieve uniform random doping over the whole sample. Also, position-selective doping has been demonstrated by combining HSQ patterning and the postdoping method. In principle, the same approach can be applied to other high-melting-point elements, such as transition metals and rare earth metals, providing opportunities to tune the Fermi level and the band structure of 2D materials. The postdoping method with controllability and broad applicability makes the present method useful to develop the next-generation 2D-semiconductor-based nanoelectronics.

EXPERIMENTAL METHODS

Sample Preparations. We prepared WSe₂ and MoSe₂ by the mechanical exfoliation or chemical vapor deposition (CVD) method on a SiO₂/Si substrate according to a previously reported procedure.³⁶ The prepared TMDs were put in a vacuum chamber (base pressure is 10⁻⁶ Pa) and were heated up to 823 K. We started supplying Se (99.999% purity, SigmaAldrich) with a Knudsen cell when the sample temperature becomes higher than 623 K to avoid unwanted formation of Se vacancies; the supply rate of Se was kept constant (2 Å/s) throughout the doping process. This preheating process makes the sample surface clean, which is required for the following metal doping process. After the preheating process, we decreased the sample temperature to 523 K and start supplying dopant (Nb or Re) with an electron beam evaporation (EFM 3, FOCUS GmbH) for 1–15 min with the supply rate 0.67–1.11 monolayer/hour.

Characterizations. Raman and PL spectra were measured with microspectroscopy systems (Jovin-Yvon HR-800 and Renishaw InVia Raman) with 488 or 532 nm CW laser excitation. The laser was focused onto samples with objective lenses (×50–100 and 0.7–0.85 NA), and Raman and PL signals were detected with a charge-coupled device (CCD). All measurements were carried out at room temperature under atmospheric conditions. Electronic properties, including transfer curves, were measured with a semiconductor parameter analyzer (Keithley 4200-SCS/F) at room temperature.

Optical responses were obtained with a homemade microspectroscopy system. HAADF- and ABF-STEM images were taken at room temperature by using a JEM-ARM200F ACCELARM (cold field emission gun) equipped with a CEOS ASCOR corrector, operated at 120 kV. For each frame of the STEM image, the fast scan rate 3–5 μs per pixel is used. Several frames up to ten are overlapped after drift compensation to form a HAADF or ABF-STEM image. EDS elemental mapping is performed by using JED-2300.

Ab Initio Calculations. The geometric and electronic structures of Nb-doped WSe₂ were investigated using the STATE package based on density functional theory.³⁷ The generalized gradient approximation with the functional forms of Perdew–Burke–Ernzerhof is adopted to describe the exchange–correlation potential energy.^{38,39} The electron–ion interaction is treated by ultrasoft pseudopotentials.⁴⁰ The valence wave function and deficit charge density were expanded by plane-wave basis sets with cutoff energies of 25 and 225 Ry, respectively. *Ab initio* molecular dynamics (MD) simulations were conducted with the use of the velocity scaling method to maintain the temperature at 300 K to implant Nb into WSe₂. Nb atom has initial velocities of 0.01, 0.3, and 1 eV toward the WSe₂ layer. *Ab initio* calculations were conducted with 2 × 2 and single γ points for static and MD calculations, respectively, under the 6 × 6 lateral periodicity of WSe₂ with Nb atom. Atomic coordinates were optimized until the force acting on each atom became less than 5 mRy/Å.

ASSOCIATED CONTENT

Supporting Information

The Supporting Information is available free of charge at <https://pubs.acs.org/doi/10.1021/acsnano.1c04584>.

Optical images of a monolayer of WSe₂ before and after Nb doping, a typical EDS spectrum and corresponding elemental mapping, the definitions of J , P_{obs} and P_{rand} , XPS spectra of a typical WSe₂ and Nb-doped WSe₂, snapshots of a Nb atom injected toward monolayer WSe₂, band structure of Nb-doped monolayer WSe₂ and corresponding wave functions, band dispersion of pristine trilayer MoSe₂ and Nb-doped trilayer MoSe₂, STM and STS observations of Nb in a Nb-doped WSe₂, and characterization of Re-doped samples (PDF)

Movie of the structural change upon injection of an Nb atom with a kinetic energy of about 300 meV toward a monolayer of WSe₂ (AVI)

AUTHOR INFORMATION

Corresponding Author

Ryo Kitaura – Department of Chemistry, Nagoya University, Nagoya, Aichi 464-8602, Japan; orcid.org/0000-0001-8108-109X; Email: r.kitaura@nagoya-u.jp

Authors

Yuya Murai – Department of Chemistry, Nagoya University, Nagoya, Aichi 464-8602, Japan

Shaochun Zhang – Department of Chemistry, Nagoya University, Nagoya, Aichi 464-8602, Japan

Takato Hotta – Department of Chemistry, Nagoya University, Nagoya, Aichi 464-8602, Japan

Zheng Liu – Innovative Functional Materials Research Institute, National Institute of Advanced Industrial Science and Technology (AIST), Nagoya, Aichi 463-8560, Japan; orcid.org/0000-0001-9095-7647

Takahiko Endo – Department of Physics, Tokyo Metropolitan University, Hachioji, Tokyo 192-0397, Japan

Hiroshi Shimizu – Department of Physics, Tokyo Metropolitan University, Hachioji, Tokyo 192-0397, Japan

Yasumitsu Miyata – Department of Physics, Tokyo Metropolitan University, Hachioji, Tokyo 192-0397, Japan

Toshifumi Irisawa – Device Technology Research Institute, National Institute of Advanced Industrial Science and Technology (AIST), Tsukuba, Ibaraki 305-8568, Japan

Yanlin Gao – Department of Physics, Graduate School of Pure and Applied Sciences, University of Tsukuba, Tsukuba 305-8571, Japan; orcid.org/0000-0002-4587-5391

Mina Maruyama – Department of Physics, Graduate School of Pure and Applied Sciences, University of Tsukuba, Tsukuba 305-8571, Japan; orcid.org/0000-0002-2872-5543

Susumu Okada – Department of Physics, Graduate School of Pure and Applied Sciences, University of Tsukuba, Tsukuba 305-8571, Japan; orcid.org/0000-0002-0783-3596

Hiroyuki Mogi – Faculty of Pure and Applied Sciences, University of Tsukuba, Tsukuba 305-8571, Japan

Tomohiro Sato – Faculty of Pure and Applied Sciences, University of Tsukuba, Tsukuba 305-8571, Japan

Shoji Yoshida – Faculty of Pure and Applied Sciences, University of Tsukuba, Tsukuba 305-8571, Japan

Hideki Shigekawa – Faculty of Pure and Applied Sciences, University of Tsukuba, Tsukuba 305-8571, Japan; orcid.org/0000-0001-9550-5148

Takashi Taniguchi – International Center for Materials Nanoarchitectonics, National Institute for Materials Science, Tsukuba 305-0044, Japan; orcid.org/0000-0002-1467-3105

Kenji Watanabe – Research Center for Functional Materials, National Institute for Materials Science, Tsukuba 305-0044, Japan; orcid.org/0000-0003-3701-8119

Ruben Canton-Vitoria – Department of Chemistry, Nagoya University, Nagoya, Aichi 464-8602, Japan

Complete contact information is available at:

<https://pubs.acs.org/10.1021/acsnano.1c04584>

Notes

The authors declare no competing financial interest.

ACKNOWLEDGMENTS

R.K. was supported by JSPS KAKENHI Grant Numbers JP16H03825, JP16H00963, JP15K13283, JP25107002, 20H05664, and JST CREST, Grant Numbers JPMJCR16F3 and JPMJCR19H4, JST SICORP Grant Number JPMJSC2110, and JST PRESTO Grant Number JPMJPR20A2. The ARPES measurements were performed at BL25SU of SPring-8 with the approval of the Japan Synchrotron Radiation Research Institute (Proposal No. 2020A1352 and 2019B1392). R.C. was supported by JSPS Grant-in-Aid for JSPS Fellows 19F19368. S.O. was supported by HSPS KAKENHI Grant Numbers JP21H05233, JP21H05232, JP21K14484, JP20K22323, JP20H00316, JP20H02080, JP20K05253, and JP20H05664. We thank T. Muro for his technical assistance during the ARPES measurement at SPring-8.

REFERENCES

- (1) Hisamoto, D.; Lee, W.; Kedzierski, J.; Takeuchi, H.; Asano, K.; Kuo, C.; Anderson, E.; King, T.; Bokor, J.; Hu, C. FinFET - A Self-Aligned Double-Gate MOSFET Scalable to 20 nm. *IEEE Trans. Electron Devices* **2000**, *47* (12), 2320–2325.
- (2) Oh, S.; Monroe, D.; Hergenrother, J. Analytic Description of Short-Channel Effects in Fully-Depleted Double-Gate and Cylindrical, Surrounding-Gate MOSFETs. *IEEE Electron Device Lett.* **2000**, *21* (9), 445–447.
- (3) Chhowalla, M.; Jena, D.; Zhang, H. Two-Dimensional Semiconductors for Transistors. *Nat. Rev. Mater.* **2016**, *1*, 16052.
- (4) Quhe, R.; Xu, L.; Liu, S.; Yang, C.; Wang, Y.; Li, H.; Yang, J.; Li, Q.; Shi, B.; Li, Y.; Pan, Y.; Sun, X.; Li, J.; Weng, M.; Zhang, H.; Guo, Y.; Xu, L.; Tang, H.; Dong, J.; Yang, J.; et al. Sub-10 nm Two-Dimensional Transistors: Theory and Experiment. *Phys. Rep.* **2021**, *938*, 1–72.
- (5) Wang, Q.; Kalantar-Zadeh, K.; Kis, A.; Coleman, J.; Strano, M. Electronics and Optoelectronics of Two-Dimensional Transition Metal Dichalcogenides. *Nat. Nanotechnol.* **2012**, *7* (11), 699–712.

(6) Jariwala, D.; Sangwan, V.; Lauhon, L.; Marks, T.; Hersam, M. Emerging Device Applications for Semiconducting Two-Dimensional Transition Metal Dichalcogenides. *ACS Nano* **2014**, *8* (2), 1102–1120.

(7) Mak, K.; Lee, C.; Hone, J.; Shan, J.; Heinz, T. Atomically Thin MoS₂: A New Direct-Gap Semiconductor. *Phys. Rev. Lett.* **2010**, *105* (13), 136805.

(8) Novoselov, K.; Geim, A.; Morozov, S.; Jiang, D.; Katsnelson, M.; Grigorieva, I.; Dubonos, S.; Firsov, A. Two-Dimensional Gas of Massless Dirac Fermions in Graphene. *Nature* **2005**, *438* (7065), 197–200.

(9) Radisavljevic, B.; Radenovic, A.; Brivio, J.; Giacometti, V.; Kis, A. Single-Layer MoS₂ Transistors. *Nat. Nanotechnol.* **2011**, *6* (3), 147–150.

(10) Li, L.; Yu, Y.; Ye, G.; Ge, Q.; Ou, X.; Wu, H.; Feng, D.; Chen, X.; Zhang, Y. Black Phosphorus Field-Effect Transistors. *Nat. Nanotechnol.* **2014**, *9* (5), 372–377.

(11) Iqbal, M.; Iqbal, M.; Khan, M.; Shehzad, M.; Seo, Y.; Park, J.; Hwang, C.; Eom, J. High-Mobility and Air-Stable Single-Layer WS₂ Field-Effect Transistors Sandwiched between Chemical Vapor Deposition-Grown Hexagonal BN films. *Sci. Rep.* **2015**, *5*, 10699.

(12) Gao, Z.; Zhou, Z.; Tomanek, D. Degenerately Doped Transition Metal Dichalcogenides as Ohmic Homojunction Contacts to Transition Metal Dichalcogenide Semiconductors. *ACS Nano* **2019**, *13* (5), 5103–5111.

(13) Bhimanapati, G.; Lin, Z.; Meunier, V.; Jung, Y.; Cha, J.; Das, S.; Xiao, D.; Son, Y.; Strano, M.; Cooper, V.; Liang, L.; Louie, S.; et al. Recent Advances in Two-Dimensional Materials beyond Graphene. *ACS Nano* **2015**, *9* (12), 11509–11539.

(14) Loh, L.; Zhang, Z.; Bosman, M.; Eda, G. Substitutional Doping in 2D Transition Metal Dichalcogenides. *Nano Res.* **2021**, *14* (6), 1668–1681.

(15) Zhang, T.; Fujisawa, K.; Zhang, F.; Liu, M.; Lucking, M.; Gontijo, R.; Lei, Y.; Liu, H.; Crust, K.; Granzier-Nakajima, T.; Terrones, H.; Elias, A.; Terrones, M. Universal *in Situ* Substitutional Doping of Transition Metal Dichalcogenides by Liquid-Phase Precursor-Assisted Synthesis. *ACS Nano* **2020**, *14* (4), 4326–4335.

(16) Pandey, S.; Alsalman, H.; Azadani, J.; Izquierdo, N.; Low, T.; Campbell, S. Controlled *p*-Type Substitutional Doping in Large-Area Monolayer WSe₂ Crystals Grown by Chemical Vapor Deposition. *Nanoscale* **2018**, *10* (45), 21374–21385.

(17) Sasaki, S.; Kobayashi, Y.; Liu, Z.; Suenaga, K.; Maniwa, Y.; Miyachi, Y.; Miyata, Y. Growth and Optical Properties of Nb-Doped WS₂ Monolayers. *Appl. Phys. Express* **2016**, *9*, 071201.

(18) Suh, J.; Park, T. E.; Lin, D. Y.; Fu, D. Y.; Park, J.; Jung, H. J.; Chen, Y. B.; Ko, C.; Jang, C.; Sun, Y. H.; Sinclair, R.; Chang, J.; Tongay, S.; Wu, J. Q. Doping against the Native Propensity of MoS₂: Degenerate Hole Doping by Cation Substitution. *Nano Lett.* **2014**, *14* (12), 6976–6982.

(19) Gao, J.; Kim, Y. D.; Liang, L. B.; Idrobo, J. C.; Chow, P.; Tan, J. W.; Li, B. C.; Li, L.; Sumpter, B. G.; Lu, T. M.; Meunier, V.; Hone, J.; Koratkar, N. Transition-Metal Substitution Doping in Synthetic Atomically Thin Semiconductors. *Adv. Mater.* **2016**, *28* (44), 9735–9743.

(20) Zhang, P.; Cheng, N. Y.; Li, M. J.; Zhou, B.; Bian, C.; Wei, Y.; Wang, X. G.; Jiang, H. N.; Bao, L. H.; Lin, Y. F.; Hu, Z. G.; Du, Y.; Gong, Y. J. Transition-Metal Substitution-Induced Lattice Strain and Electrical Polarity Reversal in Monolayer WS₂. *ACS Appl. Mater. Interfaces* **2020**, *12* (16), 18650–18659.

(21) Kretschmer, S.; Lehnert, T.; Kaiser, U.; Krashennnikov, A. V. Formation of Defects in Two-Dimensional MoS₂ in the Transmission Electron Microscope at Electron Energies below the Knock-On Threshold: The Role of Electronic Excitations. *Nano Lett.* **2020**, *20* (4), 2865–2870.

(22) Ishizuka, K. A Practical Approach for STEM Image Simulation Based on the FFT Multislice Method. *Ultramicroscopy* **2002**, *90* (2–3), 71–83.

(23) Dumcenco, D.; Kobayashi, H.; Liu, Z.; Huang, Y.; Suenaga, K. Visualization and Quantification of Transition Metal Atomic Mixing in Mo_{1-x}W_xS₂ Single Layers. *Nat. Commun.* **2013**, *4*, 1351.

(24) Hwang, B. J.; Sarma, L. S.; Chen, J. M.; Chen, C. H.; Shih, S. C.; Wang, G. R.; Liu, D. G.; Lee, J. F.; Tang, M. T. Structural Models and Atomic Distribution of Bimetallic Nanoparticles as Investigated by X-Ray Absorption Spectroscopy. *J. Am. Chem. Soc.* **2005**, *127* (31), 11140–11145.

(25) Schneider, C.; Rasband, W.; Eliceiri, K. NIH Image to ImageJ: 25 Years of Image Analysis. *Nat. Methods* **2012**, *9* (7), 671–675.

(26) Mouri, S.; Miyauchi, Y.; Matsuda, K. Tunable Photoluminescence of Monolayer MoS₂ via Chemical Doping. *Nano Lett.* **2013**, *13* (12), 5944–5948.

(27) Tang, L.; Xu, R. Z.; Tan, J. Y.; Luo, Y. T.; Zou, J. Y.; Zhang, Z. T.; Zhang, R. J.; Zhao, Y.; Lin, J. H.; Zou, X. L.; Liu, B. L.; Cheng, H. M. Modulating Electronic Structure of Monolayer Transition Metal Dichalcogenides by Substitutional Nb-Doping. *Adv. Funct. Mater.* **2021**, *31*, 2006941.

(28) Kim, J. E.; Kang, W. T.; Vu, V. T.; Kim, Y. R.; Shin, Y. S.; Lee, I.; Won, U. Y.; Lee, B. H.; Kim, K.; Phan, T. L.; Lee, Y. H.; Yu, W. J. Ideal PN Photodiode Using Doping Controlled WSe₂-MoSe₂ Lateral Heterostructure. *J. Mater. Chem. C* **2021**, *9* (10), 3504–3512.

(29) Terrones, H.; Del Corro, E.; Feng, S.; Poumirol, J.; Rhodes, D.; Smirnov, D.; Pradhan, N.; Lin, Z.; Nguyen, M.; Elias, A.; Mallouk, T.; Balicas, L.; Pimenta, M.; Terrones, M. New First Order Raman-Active Modes in Few Layered Transition Metal Dichalcogenides. *Sci. Rep.* **2015**, *4*, 4215.

(30) Wang, B.; Xia, Y.; Zhang, J.; Komsa, H.; Xie, M.; Peng, Y.; Jin, C. Niobium Doping Induced Mirror Twin Boundaries in MBE Grown WSe₂ Monolayers. *Nano Res.* **2020**, *13* (7), 1889–1896.

(31) Li, M.; Shi, Y.; Cheng, C.; Lu, L.; Lin, Y.; Tang, H.; Tsai, M.; Chu, C.; Wei, K.; He, J.; Chang, W.; Suenaga, K.; Li, L. Epitaxial Growth of a Monolayer WSe₂-MoS₂ Lateral *p-n* Junction with an Atomically Sharp Interface. *Science* **2015**, *349* (6247), 524–528.

(32) Sahoo, P.; Memaran, S.; Xin, Y.; Balicas, L.; Gutierrez, H. One-Pot Growth of Two-Dimensional Lateral Heterostructures via Sequential Edge-Epitaxy. *Nature* **2018**, *553* (7686), 63–67.

(33) Qin, Z.; Loh, L.; Wang, J.; Xu, X.; Zhang, Q.; Haas, B.; Alvarez, C.; Okuno, H.; Yong, J.; Schultz, T.; Koch, N.; Dan, J.; Pennycook, S.; Zeng, D.; Bosman, M.; Eda, G. Growth of Nb-Doped Monolayer WS₂ by Liquid-Phase Precursor Mixing. *ACS Nano* **2019**, *13* (9), 10768–10775.

(34) Feng, L.; Jiang, W.; Su, J.; Zhou, L.; Liu, Z. Performance of Field-Effect Transistors Based on Nb_xW_{1-x}S₂ Monolayers. *Nanoscale* **2016**, *8* (12), 6507–6513.

(35) Zhang, K.; Bersch, B.; Joshi, J.; Addou, R.; Cormier, C.; Zhang, C.; Xu, K.; Briggs, N.; Wang, K.; Subramanian, S.; Cho, K.; Fullerton-Shirey, S.; Wallace, R.; Vora, P.; Robinson, J. 2D Materials: Tuning the Electronic and Photonic Properties of Monolayer MoS₂ via *in Situ* Rhenium Substitutional Doping. *Adv. Funct. Mater.* **2018**, *28* (16), 1870105.

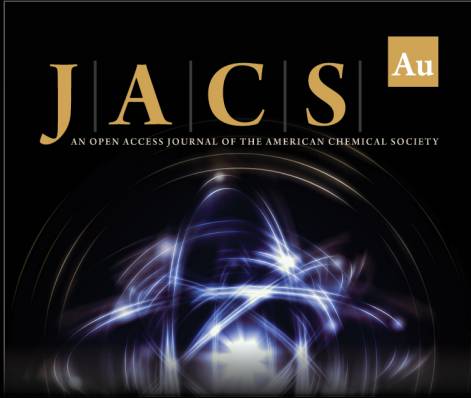
(36) Irisawa, T.; Okada, N.; Chang, W.; Okada, M.; Mori, T.; Endo, T.; Miyata, Y. CVD Grown Bilayer WSe₂/MoSe₂ Heterostructures for High Performance Tunnel Transistors. *Jpn. J. Appl. Phys.* **2020**, *59*, SGGH05–6.

(37) Morikawa, Y.; Iwata, K.; Terakura, K. Theoretical Study of Hydrogenation Process of Formate on Clean and Zn Deposited Cu(111) Surfaces. *Appl. Surf. Sci.* **2001**, *169*, 11–15.


(38) Perdew, J.; Burke, K.; Ernzerhof, M. Generalized Gradient Approximation Made Simple. *Phys. Rev. Lett.* **1996**, *77* (18), 3865–3868.


(39) Perdew, J.; Burke, K.; Ernzerhof, M. Generalized Gradient Approximation Made Simple (vol 77, pg 3865, 1996). *Phys. Rev. Lett.* **1997**, *78* (7), 1396.


(40) Vanderbilt, D. Soft Self-Consistent Pseudopotentials in a Generalized Eigenvalue Formalism. *Phys. Rev. B: Condens. Matter Mater. Phys.* **1990**, *41* (11), 7892–7895.



JACS Au
AN OPEN ACCESS JOURNAL OF THE AMERICAN CHEMICAL SOCIETY

 Editor-in-Chief
Prof. Christopher W. Jones
Georgia Institute of Technology, USA

Open for Submissions 

pubs.acs.org/jacsau  ACS Publications
Most Trusted. Most Cited. Most Read.